



HAL
open science

Ground-Based Remote Sensing and Uncertainty Analysis of the Mass Eruption Rate Associated With the 3–5 December 2015 Paroxysms of Mt. Etna

Luigi Mereu, Simona Scollo, Costanza Bonadonna, Franck Donnadieu,
Valentin Freret-Lorgeril, Frank S Marzano

► **To cite this version:**

Luigi Mereu, Simona Scollo, Costanza Bonadonna, Franck Donnadieu, Valentin Freret-Lorgeril, et al.. Ground-Based Remote Sensing and Uncertainty Analysis of the Mass Eruption Rate Associated With the 3–5 December 2015 Paroxysms of Mt. Etna. *IEEE Journal of Selected Topics in Applied Earth Observations and Remote Sensing*, 2022, 15, pp.504-518. 10.1109/JSTARS.2021.3133946 . hal-03516636

HAL Id: hal-03516636





<https://uca.hal.science/hal-03516636>

Submitted on 7 Jan 2022

HAL is a multi-disciplinary open access archive for the deposit and dissemination of scientific research documents, whether they are published or not. The documents may come from teaching and research institutions in France or abroad, or from public or private research centers.

L'archive ouverte pluridisciplinaire **HAL**, est destinée au dépôt et à la diffusion de documents scientifiques de niveau recherche, publiés ou non, émanant des établissements d'enseignement et de recherche français ou étrangers, des laboratoires publics ou privés.

Ground-Based Remote Sensing and Uncertainty Analysis of the Mass Eruption Rate Associated With the 3–5 December 2015 Paroxysms of Mt. Etna

Luigi Mereu , Simona Scollo , Costanza Bonadonna , Franck Donnadiou, Valentin Freret-Lorgeril, and Frank S. Marzano , *Fellow, IEEE*

Abstract—During explosive eruptions, the real-time estimation of the mass eruption rate (MER) is challenging although crucial to mitigate the impact of erupted tephra. Microwave radar techniques at L- and/or X-bands, as well as thermal infrared imagery, can provide a reliable MER estimation in real time. Using lava fountains of 3–5 December 2015 at Mt. Etna (Italy) as test cases, we investigate the differences among all these remote sensing methods and introduce a new approach, called the near source approach (NSA) using only X-band radar data. We also extend the volcanic advanced radar retrieval methodology to estimate the gas-tephra mixture density near the volcanic crater. The analysis of uncertainty is carried out comparing the NSA with the mass continuity approach (MCA), top plume approach (TPA) and surface flux approach (SFA), already used to estimate the MER of other Etna explosive events. The analysis allows us to identify the optimal real-time MER retrieval strategy, showing the potential and limitations of each method. We show that the MCA method, entirely based on the X-band radar data processing, is the best strategy with a percentage uncertainty in the MER estimation of 22.3%, whereas other approaches exhibit a higher uncertainty (26.4% for NSA, 30% for TPA, and 31.6% for SFA).

Index Terms—Explosive eruptions, gas-tephra mixture density, lava fountains, mass eruption rate (MER), radar and thermal data, retrieval techniques, total erupted mass (TEM), uncertainties.

I. INTRODUCTION

DURING explosive volcanic eruptions, volcanic particles of various dimensions (tephra), ranging from a few microns

Manuscript received August 6, 2021; revised November 4, 2021; accepted November 29, 2021. Date of publication December 9, 2021; date of current version January 5, 2022. This work was supported in part by the “European Network of Observatories and Research Infrastructures for Volcanology” under European Projects EUROVOLC H2020-INFRAIA-02-2017 and 731070, and in part by the funding from the European Union’s Horizon 2020 Research and Innovation Programme under Grant Agreement 731070 (EUROVOLC). (Corresponding author: Luigi Mereu.)

Luigi Mereu and Frank S. Marzano are with the Dipartimento di Ingegneria dell’Informazione (DIET), Sapienza University of Rome, 00185 Rome, Italy, and also with CETEMPS Center of Excellence, Università dell’Aquila, 67100 L’Aquila, Italy (e-mail: luigi.mereu@ingv.it; frank.marzano@uniroma1.it).

Simona Scollo is with the Istituto Nazionale di Geofisica e Vulcanologia, Osservatorio Etna, 95015 Catania, Italy (e-mail: simona.scollo@ingv.it).

Costanza Bonadonna and Valentin Freret-Lorgeril are with the Department of Earth Sciences, University of Geneva, 1205 Geneva, Switzerland (e-mail: costanza.bonadonna@unige.ch; valentin.freretlorgeril@unige.ch).

Franck Donnadiou is with the Université Clermont-Auvergne, CNRS, IRD, OPGC, Laboratoire Magmas et Volcans, F-63000 Clermont-Ferrand, France (e-mail: franck.donnadiou@uca.fr).

Digital Object Identifier 10.1109/JSTARS.2021.3133946

up to tens of centimeters, are injected into the atmosphere [1], [46]. Volcanic particles subsequently settle under the action of gravity, plume/cloud, and atmospheric dynamics [41]. Atmospheric transport of tephra, depending on particle characteristics (size, density, shape) and altitude of release, can last from minutes up to several weeks. The area affected by tephra fallout can extend thousands of square kilometers around the eruptive vent.

Recent volcanic crises, such as those associated with Eyjafjallajökull (Iceland) in 2010 and Cordón-Caulle (Chile) in 2011, have demonstrated the need for a better real-time assessment of the eruption source parameters (ESPs), namely column height, mass eruption rate (MER), total erupted mass (TEM), and total grain-size distribution. Those are in fact the main input parameters of the dispersion models, widely used to forecast the tephra dispersal and fallout during explosive eruptions. Various geophysical strategies can be applied, such as the integration among different sensors, direct observations, and field measurement analysis, in order to increase the reliability of the ESPs assessment and mitigate volcanic risks [2], [3]–[5], [42]. In particular, the MER which is a measure of the temporal rate of magmatic flow through the volcano vent [6].

Mt. Etna, in Italy, is one of the most active volcanoes in the world, whose explosive eruptions represent a serious threat to the communities located around it, producing various dangerous effects on inhabitants, properties, and communication routes, and at the same time represents an ideal laboratory to improve volcano monitoring and forecasting of eruptive events [7]. The summit of Etna is made up of three main craters: Voragine Crater (VOR), NorthEast Crater (NEC), and SouthEast Crater (SEC), as shown in Fig. 1(a). From 2009 to 2013, the explosive activity was located on the east flank of SEC, which formed a new pyroclastic cone named New SouthEast Crater (NSEC) [8]. Fig. 1(b) also shows the map of the network of sensors used in this work. Each sensor is marked with colored dots. In particular, the observations are obtained by the following.

(1) The X-band weather radar (XWR), at about 32 km from the VOR, which is a dual-polarization scanning radar of the Italian weather radar network, already successfully used to retrieve ESPs [9], [20], [47]. This radar operates at 9.6 GHz, with transmitted peak power of 50 kW, half-power beam width of 1.3 degree, and considering a permittivity factor of tephra particles equal to 0.39 with respect to 0.93 for water particles

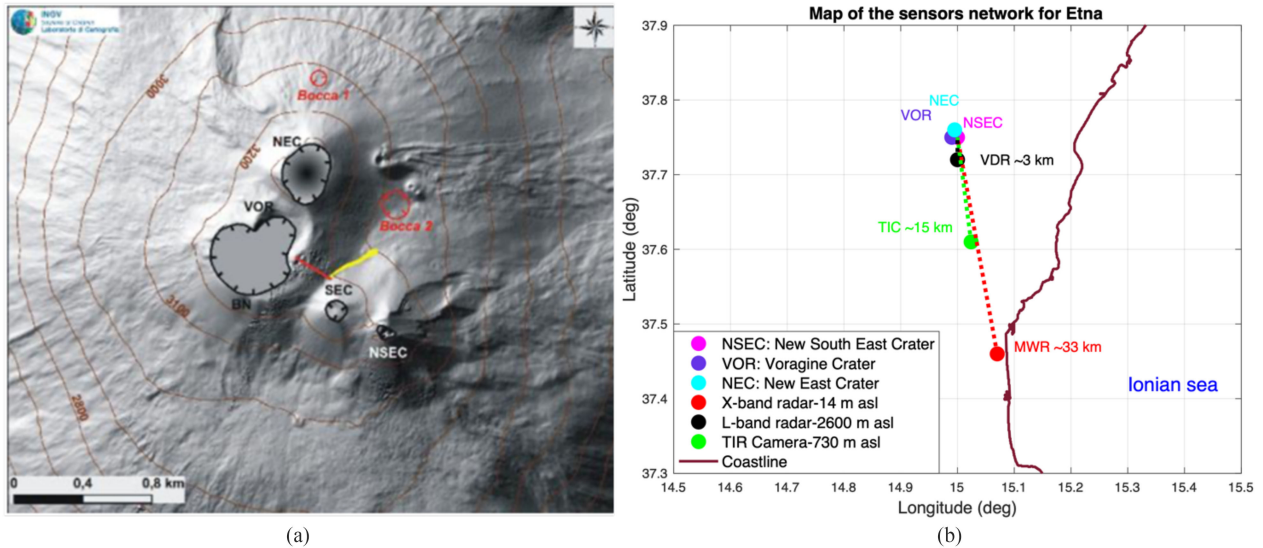


Fig. 1. (a) Map of the main craters of Etna volcano: Voragine Crater (VOR), North-East Crater (NEC), New Southeast Crater (NSEC), Southeast Crater (SEC). (b) Map of the sensor network used in this work is shown. Each sensor and crater are geolocated in terms of latitude and longitude and highlighted with colored dots, specifying the elevation above sea level (asl), as listed in the legend. The colored dashed lines show the distance between each sensor and the Etna summit, as clarified for each one in km.

[25]. The XWR performs a 3-D scan of the surrounding scene as a function of range, azimuth, and elevation with five azimuthal scans per minute.

(2) The fixed-pointing L-band Doppler radar VOLDORAD-2B (VDR, wavelength of 23.5 cm) for the near-crater detection of erupted material during Etna’s explosive events. This Doppler radar measures both the radial velocity v_r and the received backscattered power that characterizes the amount of detected tephra at high-time resolution (i.e., 0.2 s; cf. open-access data base used in this study [44]). From the observation geometry, it is possible to convert v_r into exit velocity v_{ex} (i.e., $v_{ex} = 3.89 v_r$) ([31], [21], [45]), whereas from the specifications of the L-band radar and the radar constant, the backscattered power can be transformed into the L-band reflectivity factor Z_{hh} [14].

(3) The thermal infrared camera (TIC), which is located at 15 km, in Nicolosi [13], on the south flank of Etna and belongs to the video-monitoring network system of the INGV-OE. TIC provides a time series of 640×480 pixels images with a spatial resolution of a few meters and a thermal sensitivity of 80 mK at 25°C. The images are displayed with a fixed color scale with a range of -10°C to 70°C [13].

The MER is fundamental to accurately forecast the eruptive column evolution and the ash cloud dispersal. During a volcanic crisis, direct remote sensing measurements can provide information on the ongoing activity and allow evaluating the impact of an explosive event [17]. However, the uncertainty related to the ESPs is difficult to assess due to the variability of instrument features and parameters used in the methodology. In general, the reliability in the uncertainty estimation depends on the degrees of freedom, or on the independent quantities that contribute to the MER estimates.

In this work, following and extending previous studies [4], [6], [18], [21], we estimate the MER derived from the XWR, VDR, and TIC, and analyze in detail the various methodologies applied to the four Etna lava fountains occurred in 3–5 December 2015.

We select this case study mainly because the observations of the three different sensors, described previously, are available at the same time. Starting from previous studies ([6], [18], [37], [42]), we aim at the following:

- 1) describing a new MER approach (Near Source Approach - NSA), which completes the set of the proposed methods;
- 2) comparing multisensor strategies for MER determination;
- 3) identifying the limits, advantages, and uncertainties correlated to each methodology;
- 4) exploring the possibility to integrate different approaches to estimate the MER;
- 5) calculating the gas-tephra mixture density near the eruptive vent and the relative uncertainty; and
- 6) identifying the best integrated strategy to reduce errors in MER retrievals.

The rest of this article is organized as follows. Section II illustrates the Etna 2015 paroxysm observations by XWR, VDR, and TIC sensors. Section III describes the different MER methodologies used and relative uncertainties. Section IV is devoted to the MER retrievals and relative uncertainties, while Section V summarizes the MER results. Finally, Section VI concludes this article.

II. ETNA 2015 LAVA FOUNTAINS OBSERVATIONS

Between the early morning of 3 December and the afternoon of 5 December 2015, four powerful paroxysmal events were produced from the VOR crater. These events generated tall lava fountains above the crater and tephra plumes up to 12–16 km (all heights are asl) [38], observed by the XWR, VDR, and TIC, at the same time.

A. Thermal Infrared Observations

In the first third of the volcanic plumes, we clearly identify a jet, called the incandescent jet region (IJR), which is mainly

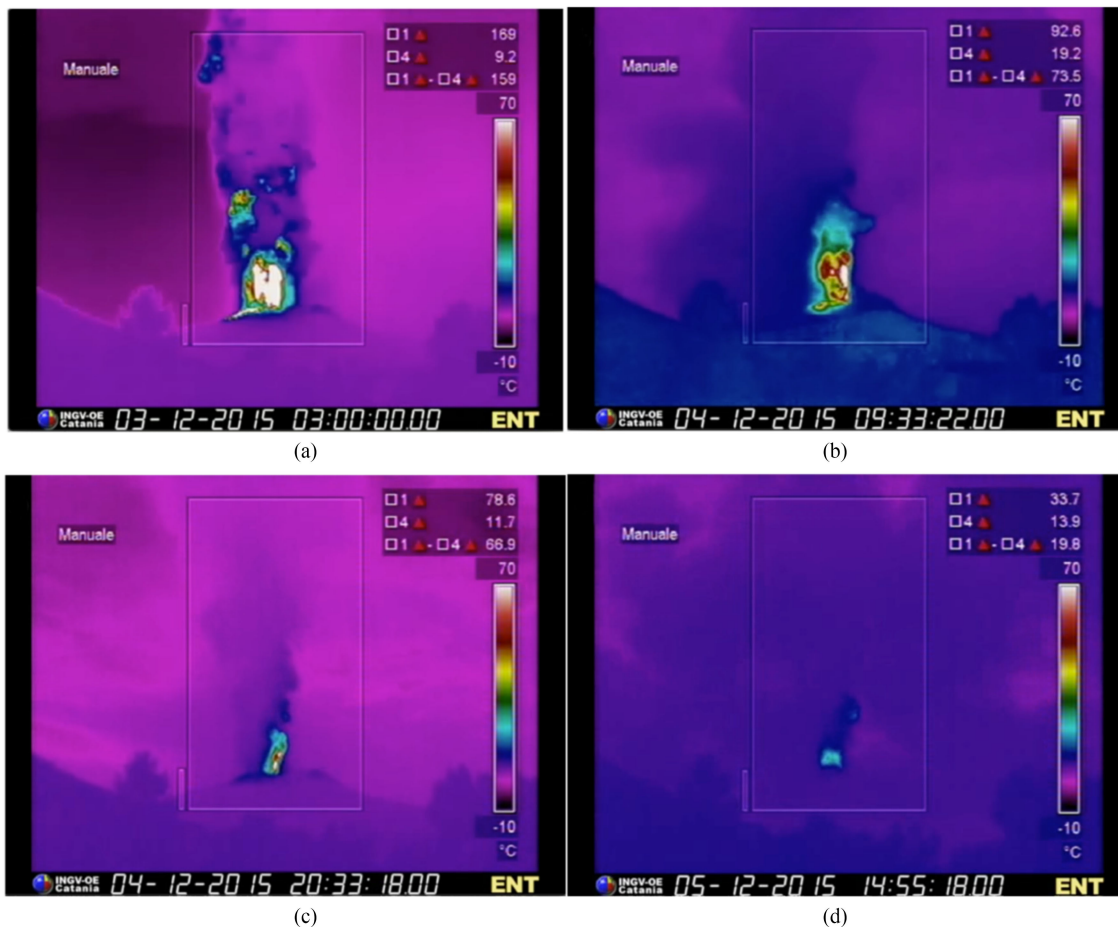


Fig. 2. Frames of the thermal infrared camera in Nicolosi (named ENT) showing the lava fountains at the VOR on 3–5 December 2015, panels (a), (b), (c), and (d), respectively. Below each image, the date (dd-mm- yyyy) and UTC time (hh:mm:ss:00) of the Etna eruptive events. The color bar on the right side of each picture shows the uncalibrated temperature ranging between -10°C and 70°C .

composed of lapilli and bombs mixed with hot gas [1], [48]. Most procedures, used to identify the IJR, are based on setting a suitable threshold to the vertical spatial gradients and/or to edge-contour detection filters on thermal images [37], [49]. By selecting the TIC frames at time intervals of 1 min, it is possible to derive the IJR top height in each image, as described in [12], [15], [29], [31], [32], and [37].

In Fig. 2 we show the main frames displaying the lava fountains associated with the eruptive sequence occurring on: 1) 3 December 2015 at 03:00 UTC; 2) 4 December 2015 at 09:30 UTC; 3) 4 December 2015 at 21:00 UTC; and 4) 5 December 2015 at 15:30 UTC.

B. Microwave Observations

The comparative analysis of the XWR measurements provides the first interesting information on the vertical structure of the tephra plume. Focusing on the eruptive observations, Fig. 3 shows the vertical and horizontal maps of the four eruptive events analyzed in this work. We show the Plan Position Indicator (PPI) of XWR reflectivity factor Z_{hh} (dBZ) at 6° elevation radar (a1), (a2), (a3), and (a4); vertical cut of the copolar reflectivity factor Z_{hh} (dBZ) along the line connecting the radar site and the

maximum horizontal ash plume extension (b1), (b2), (b3), and (b4). Regarding the PPI, the wind action in altitude is clearly perceivable, which can project the space-time evolution of the eruptive cloud in different directions of the horizon. In the panels (b1–b4) the top plume altitude H_{TP} is clearly identifiable between 12–16 km and the plume is displaced with respect to the vertical line centered on the eruptive vent.

Fig. 4 shows the overlapping between the maximum values Z_{hh} detected both by the XWR (red line) about 33 km far from the VOR crater, i.e., at the fifth elevation angle, and detected by the VDR (about 4 km from VOR), each 30 s (green line) and averaged over 10 min (blue lines). For the three events on 4 and 5 December, there is a qualitative match between both radar Z_{hh} trends with maximum values slightly exceeding 60 dBZ [see Fig. 4(b)–(d)]. For the most powerful event on 3 December, the VDR trend of Z_{hh} exceeds the XWR estimates with values of about 70 against 60 dBZ (see Fig. 4(a)).

The main features for each event of the 2015 Etna eruption are listed in Table I, as well as the temporal duration, the top plume altitude H_{TP} (asl) and the VARR-estimated tephra classes. The maximum H_{TP} value is detected both from ground-based XWR data and from satellite spectroradiometers [36]. During the 4 and 5 December cases, the satellite-based H_{TP} is higher than

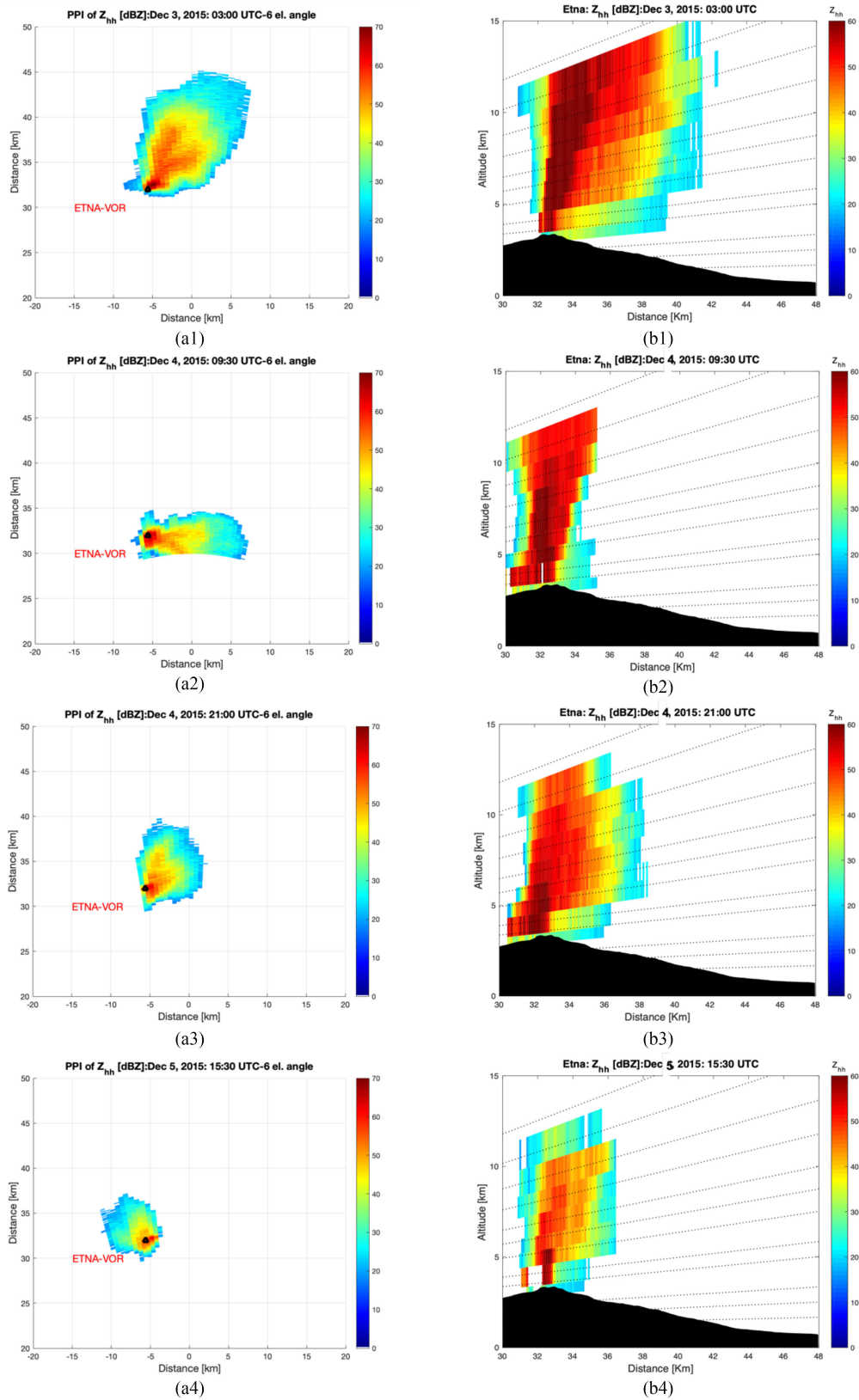


Fig. 3. X-band radar data of Etna explosive events on (a1, b1) 3 December 2015 at 03:00 UTC; (a2, b2) 4 December 2015 at 09:30 UTC; (a3, b3) 4 December 2015 at 21:00 UTC; and (a4, b4) 5 December 2015 at 15:30 UTC. We can observe the PPI of copolar radar reflectivity factor Z_{hh} (dBZ) at 6° elevation radar (panels a1–a4) and the RHI of the copolar radar reflectivity factor Z_{hh} (dBZ) of XWR (panels b1–b4).

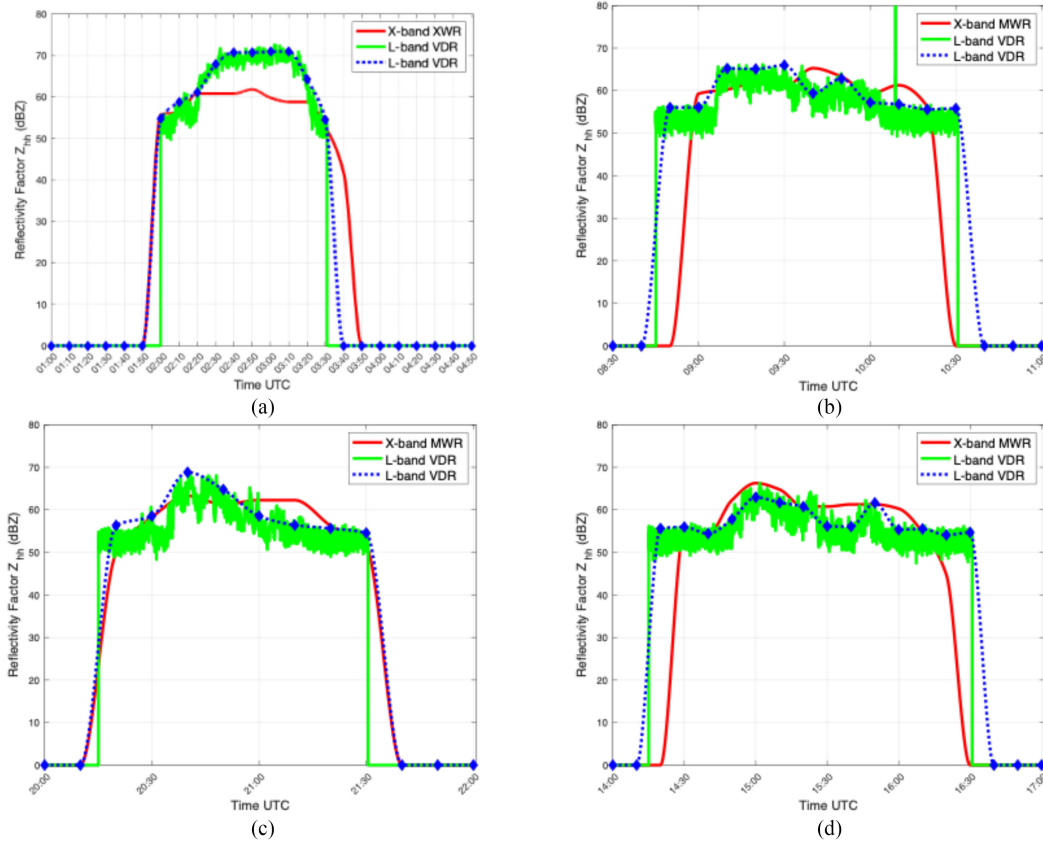


Fig. 4. Radar reflectivity factor time series of the four Etna explosive events on (a) 3 December 2015; (b) 4 December 2015; (c) 4 December 2015 and; (d) 5 December 2015. Each curve is related to the bin volume near the summit crater, that is the fifth elevation angle for the XWR and eighth and ninth range bins for the VDR, considering that the latter points directly near to the volcanic source of VOR. The reflectivity factor Z_{hh} (dBZ) derived from the XWR is sampled every 10 min (red line) and from the VDR directly every 30 s (green line) or linearly interpolated every 10 min (dotted blue line).

TABLE I

ETNA ERUPTION FEATURES ON 3–5 DECEMBER 2015, DERIVED FROM THE XWR ELABORATION APPLYING THE VARR METHODOLOGY AND FROM LITERATURE

| Eruption features | 3 December 2015 | 4 December 2015 | 4 December 2015 | 5 December 2015 |
|--|-----------------|-----------------|-----------------|-----------------|
| Duration UTC (*) | 02:20-03:45 | 08:30-10:30 | 19:50-21:15 | 14:25-17:20 |
| Top Plume altitude (*) | ~12.5 | ~17.6 | ~16.1 | ~14.1 |
| Top Plume altitude (**) | ~14.6 | ~13.1 | ~13.3 | ~13.1 |
| asl H_{TP} (km) (***) | ~15.5 | ~13.5 | ~13.5 | ~12.6 |
| Tephra classes (**): | | | | |
| CA (D_n: 0.064 mm-2 mm) | 62.5% | 77.5% | 69% | 89.5% |
| FL (D_n: 2 mm-4 mm) | 36% | 22% | 30% | 10.5% |
| ML (D_n: 4 mm- 16 mm) | 0% | 0% | 0% | 0% |
| LL (D_n: 16 mm-65 mm) | 1.5% | 0.5% | 1% | 0% |
| (*): Corradini et al. (2018); (**): VARR (X-band MWR); (***): Vulpiani et al., 2016; | | | | |

the XWR one (about 17.6 km versus 13.1 km and 14.1 km versus 13.1 km, respectively, for the satellite [36] and XWR [6], [20]). This trend is reversed on 3 December, where we find 12.5 and 14.6 km for the satellite and XWR, respectively, probably due to the effect of larger tephra particles. The four eruptive columns measured by XWR are generally composed of more than 60% of coarse ash (CA). For the first two events, proportions of 10–30% and less than 2% are found for fine Lapilli (FL) and large Lapilli (LL), respectively [25], [37].

III. MASS ERUPTION RATE METHODOLOGIES AND UNCERTAINTIES

The block diagram of the extended VARR algorithm to implement the four MER (hereafter indicated with Q_M) methods and derive the input parameters used in each approach is shown in Fig. 5. Some MER retrieval methods, already described in previous works [4], [6], [25], [37], are based on the analysis of observations collected by XWR, VDR, and TIC sensors. The four approaches to estimate MER are as follows:

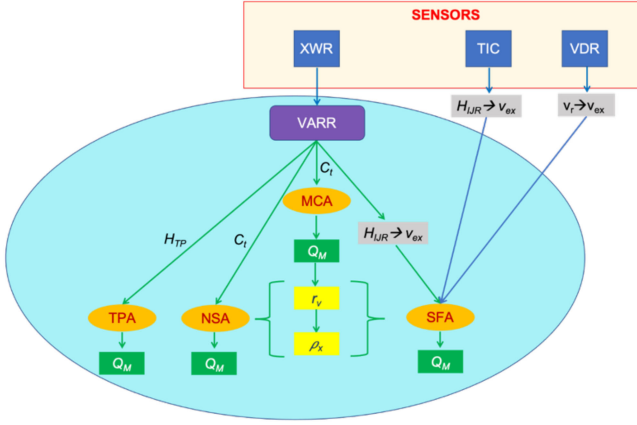


Fig. 5. Flow diagram of extended VARR algorithm, which starting from the sensors data, allows to implement the four methodologies for the Q_M estimation (i.e., MER).

- 1) Mass continuity approach (MCA), related to time-space variation of mass concentration of the whole plume detected by the XWR [6], [18], [37].
- 2) NSA, correlated to tephra concentration variation in the beam lower surface nearest to the summit crater, obtained by XWR. This Q_M estimation method is new and based entirely on the XWR measurements, adapted from [20] and [42].
- 3) Top Plume Approach (TPA), using semiempirical parametric models integrating the top plume altitude derived from XWR [18], [6], [33].
- 4) Surface Flux Approach (SFA), that links the MER to the exit velocity v_{ex} , derived from XWR, VDR, or TIC [18], [37]. The gas-tephra mixture density is estimated using the XWR technique.

For each method, we show the percentage uncertainty $\varepsilon_Q = 100(\delta Q_M/Q_M)$, evaluated according to the first-order error propagation theory for each independent variable [18].

A. Mass Continuity Approach (MCA)

The general approach starts from the conservation of mass, as described in [6], [18], [37]. The *a priori* hypotheses used to compute the MER are: (i) no source–sink term; (ii) negligible advection; and (iii) time sampling of radar. Assuming a space-time discretization related to the XWR operating mode, the MER can be expressed as follows:

$$Q_M^{(MCA)}(t) \cong Q_{M\text{dif}}(t) + Q_{M\text{adv}}(t) \quad (1)$$

where $Q_{M\text{dif}}(t)$ is correlated to the variation in each radar volume bin between two consecutive sampling times, and the $Q_{M\text{adv}}(t)$ is linked to the thrust flow outside the plume volume [6]. The latter term is mainly related to the XWR horizontal velocity deduced from the cross-correlation between two consecutive XWR vertical–horizontal section of the eruptive event. To optimize the Q_M estimates, we identify the maximum volume involved in the eruptive plume, as detected by the XWR. We search for the base

area of the volume, centered over the Etna crater (i.e., VOR in our test), which optimizes the Q_M estimates.

The overall uncertainty $\varepsilon_Q^{(MCA)}$ (7) as reported in [18] and shown in Table IV is estimated using the error propagation theory for independent errors, and is equal to 22.3% in relative percentage, assuming the variations $\delta Q_{M\text{dif}} = 0.20Q_M$ and $\delta Q_{M\text{adv}} = 0.10Q_{M\text{adv}}$ (see Table V). The advantage of this technique is the use of the direct XWR observables, making this approach applicable in near-real time.

B. Near Source Approach (NSA)

A further method, employing parameters derived by processing XWR measurements, can be introduced. The tephra concentration C_t , derived from the VARR technique [4], [6], [37], [18], is the input parameter used in the near surface approach (NSA) as well as v_{ex} and the area of the eruptive flow near the VOR crater as detected from the XWR scans [20].

We can define A_{NS} as the near source area above the crater when C_t is greater than a fixed threshold value. This area is related to the radar bins above the VOR, i.e., corresponding to the fourth and fifth elevation angle of the XWR in which the erupted mass flow is more intense. We calculate the Q_M starting from the integration of C_t flowing with v_{ex} through the elementary area dA of A_{NS} , as defined in the following relation:

$$Q_M^{(NSA)}(t) = \int_{A_{NS}} C_t(t) v_{ex}(t) dA \quad (2)$$

where v_{ex} is derived from H_{IJR} as discussed previously [37]. The advantage of this method is that each parameter is derived independently from the XWR alone and, for this reason, it can be applied in real time.

In the same way as before, the uncertainty $\varepsilon_Q^{(NSA)}$ is computed assuming for each independent parameter the following variations: $\delta C_t = 0.10C_t$, $\delta H_{IJR} = 0.20H_{IJR}$, and $\delta A_{NS} = 0.20A_{NS}$. Consequently, the relative percentage error ε_Q is equal to 26% (see Table V).

C. Top Plume Approach (TPA)

Different nonlinear parametric relations between Q_M and top plume H_{TP} are known in literature [1], [10], [22], [26], [28], [33], [35]. In this work, we consider the model of Degruyter and Bonadonna, 2012, (DB12) [33], that includes both the wind and buoyancy contributions at a given instant [6], using the following relation:

$$Q_M^{(TPA)}(t) = \alpha H_{TP}^4 + \beta H_{TP}^3 \quad (3)$$

where α , β are two variables that include a series of environmental parameters. For the considered case studies, a wind velocity of 7 m/s is obtained, averaging the wind velocity derived from the radio-sounding (Trapani observations) along the vertical altitude from the VOR and the maximum altitude reached by the volcanic plume.

The uncertainty $\varepsilon_Q^{(TPA)}$ in this case is equal to 30%, assuming for each independent variable the following variations: $\delta\alpha = 0.20\alpha$, $\delta\beta = 0.20\beta$, and $\delta H_{TP} = 0.20H_{TP}$ (see Table V).

TABLE II
AVERAGED VALUES OF $\overline{Q_M}$ (kg/s) AND $\overline{Q_V}$ (m³/s) OVER THE ENTIRE DURATION OF ETNA'S PAROXYSMS ON 3–5 DECEMBER 2015

| Model-Sensor | $\overline{Q_M}$ (kg/s) | | | | $\overline{Q_V}$ (m ³ /s) | | | |
|---|----------------------------------|----------------------------------|----------------------------------|----------------------------------|--------------------------------------|----------------------------------|----------------------------------|----------------------------------|
| | 2015-12-03 01.00-04:50 UTC | 2015-12-04 08.30-11:00 UTC | 2015-12-04 20.00-22:00 UTC | 2015-12-05 14.30-17:00 UTC | 2015-12-03 01.00-04:50 UTC | 2015-12-04 08.30-11:00 UTC | 2015-12-04 20.00-22:00 UTC | 2015-12-05 14.30-17:00 UTC |
| a) TPA-DB12 D&B 2012 (7 m/s) | 8.8 10 ⁵ | 6.5 10 ⁵ | 5.1 10 ⁵ | 3.9 10 ⁵ | 3.3 10 ² | 2.4 10 ² | 1.9 10 ² | 1.5 10 ² |
| b) SFA - TIC | 6.5 10 ⁵ | 4.7 10 ⁵ | 1.4 10 ⁵ | 2.3 10 ⁵ | 2.4 10 ² | 1.8 10 ² | 0.5 10 ² | 0.8 10 ² |
| c) SFA - XWR | 5.8 10 ⁵ | 5.1 10 ⁵ | 3.9 10 ⁵ | 6.0 10 ⁵ | 2.2 10 ² | 1.9 10 ² | 1.4 10 ² | 2.2 10 ² |
| d) SFA - VDR | 4.5 10 ⁵ | 3.1 10 ⁵ | 2.6 10 ⁵ | 2.6 10 ⁵ | 1.7 10 ² | 1.2 10 ² | 1.0 10 ² | 1.0 10 ² |
| e) MCA - XWR ($Q_{Mdif} + Q_{Madv}$) | 10.1 10 ⁵ | 4.3 10 ⁵ | 3.3 10 ⁵ | 2.6 10 ⁵ | 3.8 10 ² | 1.6 10 ² | 1.2 10 ² | 1.0 10 ² |
| f) NSA - XWR | 5.5 10 ⁵ | 4.5 10 ⁵ | 4.4 10 ⁵ | 1.8 10 ⁵ | 2.0 10 ² | 1.7 10 ² | 1.4 10 ² | 0.7 10 ² |
| g) Vulpiani et al. 2016 | 12.5 10 ⁵ | 5.0 10 ⁵ | 3.1 10 ⁵ | 2.7 10 ⁵ | 4.6 10 ² | 1.9 10 ² | 1.2 10 ² | 1.0 10 ² |
| h) Freret-Lorgeril et al. 2018 | 14.5 10 ⁵ | 1.2 10 ⁵ | 1.4 10 ⁵ | 0.8 10 ⁵ | 5.4 10 ² | 0.4 10 ² | 0.5 10 ² | 0.3 10 ² |
| i) Freret-Lorgeril et al. 2018 -Climax | 27.0 10 ⁵ | 2.2 10 ⁵ | 3.7 10 ⁵ | 1.6 10 ⁵ | 10 10 ² | 0.8 10 ² | 1.4 10 ² | 0.6 10 ² |

Note: (a) Applying the TPA parametric models DB12; (b, c, and d) using the SFA method ingesting the XWR, VDR, and TIC data; (e) implementing the MCA, (f) NSA approaches, and (g, h, and i) derived from literature. The Case i) is related to climax for each event on 3–5 December 2015, that is 02:32–03:12 UTC, 09:07–09:30 UTC, 20:36–20:50 UTC, and 14:54–15:25 UTC.

TABLE III
SAME AS TABLE II BUT SHOWING THE TEM AND TEV, RESPECTIVELY, IN (kg) AND (m³)

| Model-Sensor | TEM (kg) | | | | TEV (m ³) | | | |
|---|----------------------------------|-------------------------------|----------------------------------|----------------------------------|----------------------------------|----------------------------------|----------------------------------|----------------------------------|
| | 2015-12-03 01.00-04:50 UTC | 2015-12-04 08.30-11:00 UTC | 2015-12-04 20.00-22:00 UTC | 2015-12-05 14.30-17:00 UTC | 2015-12-03 01.00-04:50 UTC | 2015-12-04 08.30-11:00 UTC | 2015-12-04 20.00-22:00 UTC | 2015-12-05 14.30-17:00 UTC |
| a) TPA-DB12 D&B 2012 (7 m/s) | 12.7 10 ⁹ | 6.3 10 ⁹ | 4.0 10 ⁹ | 4.6 10 ⁹ | 4.7 10 ⁶ | 2.3 10 ⁶ | 1.5 10 ⁶ | 1.7 10 ⁶ |
| b) SFA - TIC | 9.4 10 ⁹ | 4.6 10 ⁹ | 1.1 10 ⁹ | 2.6 10 ⁹ | 3.5 10 ⁶ | 1.7 10 ⁶ | 0.4 10 ⁶ | 1.0 10 ⁶ |
| c) SFA - XWR | 8.4 10 ⁹ | 4.9 10 ⁹ | 3.0 10 ⁹ | 6.8 10 ⁹ | 3.1 10 ⁶ | 1.8 10 ⁶ | 1.1 10 ⁶ | 2.5 10 ⁶ |
| d) SFA - VDR | 6.5 10 ⁹ | 3.0 10 ⁹ | 2.0 10 ⁹ | 2.9 10 ⁹ | 2.4 10 ⁶ | 1.1 10 ⁶ | 0.7 10 ⁶ | 1.1 10 ⁶ |
| e) MCA - XWR ($Q_{Mdif} + Q_{Madv}$) | 7.3 10 ⁹ | 2.0 10 ⁹ | 1.3 10 ⁹ | 1.5 10 ⁹ | 2.7 10 ⁶ | 0.8 10 ⁶ | 0.5 10 ⁶ | 0.5 10 ⁶ |
| f) NSA - XWR | 7.9 10 ⁹ | 4.3 10 ⁹ | 3.4 10 ⁹ | 4.3 10 ⁹ | 2.0 10 ⁶ | 1.6 10 ⁶ | 1.3 10 ⁶ | 0.8 10 ⁶ |
| g) Vulpiani et al. 2016 | (6.3-9.1) 10 ⁹ | (2.4-2.6) 10 ⁹ | (1.1-1.2) 10 ⁹ | (1.1-1.2) 10 ⁹ | (2.3-3.4) 10 ⁶ | (0.9-1.0) 10 ⁶ | (0.4-0.5) 10 ⁶ | (0.4-0.5) 10 ⁶ |
| h) Freret-Lorgeril et al. 2018 | 7.9 10 ⁹ | 0.5 10 ⁹ | 0.4 10 ⁹ | 0.4 10 ⁹ | 2.9 10 ⁶ | 0.2 10 ⁶ | 0.1 10 ⁶ | 0.1 10 ⁶ |
| i) Freret-Lorgeril et al. 2018 -Climax | 6.5 10 ⁹ | 3.0 10 ⁹ | 0.3 10 ⁹ | 0.3 10 ⁹ | 2.4 10 ⁶ | 1.1 10 ⁶ | 0.1 10 ⁶ | 0.1 10 ⁶ |

D. Surface Flow Approach (SFA)

The divergence theorem allows us to transform a volume integral of the vector divergence into an integral area over the surface that defines the volume of the detected plume from the XWR [6], [20]. We select the nearest area to the volcanic vent where v_{ex} is normal to the surface $S_v = (\pi \cdot r_v^2)$ and under a spatial uniform flow assumption, we estimate Q_M as follows:

$$Q_M^{(SFA)}(t) \cong \rho_x v_{ex}(t) S_v \quad (4)$$

where ρ_x is the density (kg/m³) of the erupted mixture that can be assumed (i.e., from literature) or retrieved from the XWR and r_v is the vent radius (m) assuming a circular vent shape.

We can estimate the vent radius r_v implementing the regressive power law for circular vent shape, as in the case of Etna, derived from Wilson and Head (1981), correlating this quantity with the MCA Q_M . In the relation $r_v = cQ_M^d$, the variables c (0.01709, 0.007967, 0.01149) and d (0.4331, 0.4902, 0.4819) are the regressive coefficients, varying as a function of the exsolved water content w_t (0.75%, 0.20%, and 0.06%, respectively) [29] (see Fig. 6). The regressive correlation is computed also considering a fissure with length L and the same exsolved water content. Taking from the MCA, a Q_M of 10⁶ kg/s, the r_v can be assumed to be around 10 m [1], [29]. This radius estimate is confirmed by analyzing the thermal-infrared images measuring the average size of the detected vertical column [18]. The uncertainty $\varepsilon_Q^{(SFA)}$ is equal to 31.6% as previously described in (5) in [18] and shown in Table V, while the assumptions relating to the mixture density

TABLE IV
 SUMMARY TABLE OF Q_M METHODS WITH RELATIVE EQUATION AND ESTIMATED UNCERTAINTY

| Q_M Methods | Q_M Equation | Uncertainty $\varepsilon_Q = (\delta Q_M / Q_M)$ | Uncertainty values (%) |
|---------------|--|--|--|
| MCA | $Q_{Mdif}(t) + Q_{Madv}(t)$ | $\sqrt{\left(\frac{\delta Q_{Mdif}}{Q_M}\right)^2 + \left(\frac{\delta Q_{Madv}}{Q_M}\right)^2}$ | $\delta Q_{Mdif} = 0.20Q_M$ $\delta Q_{Madv} = 0.10Q_{Madv}$ $\varepsilon_Q = 22.3\%$ |
| NSA | $\int_{A_{NS}} C_t(t) v_{ex}(t) dA_{NS}$ | $\sqrt{\left(\frac{\delta C_t}{C_t}\right)^2 + \left(\frac{\delta H_{IJR}}{H_{IJR}}\right)^2 + \frac{1}{2}\left(\frac{\delta r_v}{r_v}\right)^2}$ | $\delta C_t = 0.10C_t$ $\delta H_{IJR} = 0.20H_{IJR}$ $\delta r_v = 0.20r_v$ $\varepsilon_Q = 26.4\%$ |
| TPA | $\alpha H_{TP}^4(t) + \beta H_{TP}^3(t)$ | $\sqrt{\left(\frac{\delta \alpha}{\alpha}\right)^2 + \frac{1}{4}\left(\frac{\delta H_{TP}}{H_{TP}}\right)^2 + \left(\frac{\delta \beta}{\alpha \beta}\right)^2}$ | $\delta \alpha = 0.20\alpha$ $\delta \beta = 0.20\beta$ $\delta H_{TP} = 0.20H_{TP}$ $\varepsilon_Q = 30\%$ |
| SFA | $\rho_x(t) v_{ex}(t) S_v$ | $\sqrt{\left(\frac{\delta \rho_x}{\rho_x}\right)^2 + \left(\frac{\delta H_{IJR}}{H_{IJR}}\right)^2 + \frac{1}{2}\left(\frac{\delta r_v}{r_v}\right)^2}$ | $\delta \rho_x = 0.20\rho_x$ $\delta r_v = 0.20r_v$ $\delta H_{IJR} = 0.20H_{IJR}$ $\varepsilon_Q = 31.6\%$ |

 TABLE V
 CORRELATION COEFFICIENTS MATRIX COMPUTED AMONG THE Q_M METHODS: MCA, NSA, TPA, SFA-VDR, AND SFA-TIC FOR ALL THE 2015 ETNA LAVA FOUNTAIN EVENTS ANALYZED IN THIS WORK

| Correlation | MCA | NSA | TPA | SFA-VDR | SFA-TIC | SFA-XWR |
|-------------|------|------|------|---------|---------|---------|
| MCA | 1.00 | 0.69 | 0.86 | 0.92 | 0.74 | 0.77 |
| NSA | 0.69 | 1.00 | 0.81 | 0.76 | 0.44 | 0.69 |
| TPA | 0.86 | 0.81 | 1.00 | 0.94 | 0.61 | 0.78 |
| SFA-VDR | 0.92 | 0.76 | 0.94 | 1.00 | 0.71 | 0.87 |
| SFA-TIC | 0.74 | 0.44 | 0.61 | 0.71 | 1.00 | 0.67 |
| SFA-XWR | 0.77 | 0.69 | 0.78 | 0.87 | 0.67 | 1.0 |

Note: The positive values, ranging between 0 and 1, are identified by different colored boxes: green per the maximum value (>0.9) and red (<0.5).

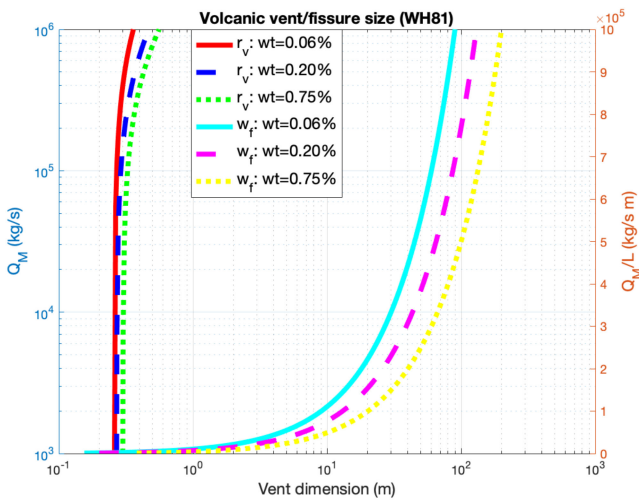


Fig. 6. Variation of the circular vent radius r_v with Q_M and surface fissure width w_f with Q_M/L [mass eruption rate per unit length of fissure for an elongated vent applying the Wilson and Head (1981) relation as a function of the exsolved water content wt of 0.75%, 0.20%, and 0.06% (red, blue, and green; and cyan, magenta, and yellow solid and dashed lines, respectively)].

are reported in the next paragraph. It is worth noting that, once r_v is estimated, the gas-tephra mixture density ρ_x can be retrieved starting from the $Q_M^{(MCA)}$ independent retrievals derived from the MCA and the estimations of v_{ex} . The mixture density ρ_x is much greater than the ambient air when the gas-mass fraction is small, but decreases rapidly during entrainment, as the gas-mass fraction increases. At high temperatures, the gas is heated by the solids, expands, and has a very low density. As a result, even with dense solid particles, the mixture density becomes substantially less than the environment. As air is added, the mixture density eventually attains a minimum.

As more air is added, the density tends toward the original density of the surrounding atmosphere, since the mass fraction of ash present is so small that its effect becomes negligible [1]. Generally, the density of a well-mixed parcel of hot tephra, as magmatic gas and air, varies according to the temperature and particle fraction of pyroclasts in the mixture [5], [15], [28]. As reported in [18], lava fountains are characterized by a range of gas content between 2% and 3% [9], [12], [19], a gas density of 0.15 kg/m^3 , and a magma density of 2700 kg/m^3 [3], resulting in a gas-tephra mixture density ρ_x in the rising part of the conduit

between 5–15 kg/m³ [16], [32]. An estimate of ρ_x for the events considered herein is about 7.5 kg/m³.

Indeed, we can retrieve ρ_x inverting (4), knowing $Q_M^{(MCA)}$, r_v , and v_{ex}

$$\hat{\rho}_x = Q_M^{(MCA)} \frac{1}{\pi r_v^2 v_{ex}}. \quad (5)$$

The tephra exit velocity v_{ex} in (5) is sonic and nearly independent of the crater pressure, but the crater pressure and hence the mixture density is closely coupled to the mass eruption rate and thus to the vent radius [1]. In this study, we consider v_{ex} derived from each sensor. 1) SFA based on the XWR v_{ex} retrievals. Applying the methodology discussed in [37], which combines the opposite trend between radar reflectivity and correlation coefficient, we derive the $H_{I,JR}$. The tephra exit velocity v_{ex} is then derived inverting the Bernoulli relation [18], [20]. 2) SFA based on VDR v_{ex} retrievals. The VDR provides the maximum positive Doppler velocity $V_{max}^+(t)$, that is geometrically correlated to the ejection velocities v_{ex} assuming vertical jets [11], [21], [30], [31], [45]. 3) SFA based on TIC v_{ex} retrievals. Applying a temperature gradient algorithm on TIC images, as discussed in [18] and [37], we identify the $H_{I,JR}$ used to derive the v_{ex} applying the Bernoulli equation. A possible limit could be due only to the reduced TIC visibility due to the superimposition of meteorological clouds on the scene under observation. The uncertainty correlated to gas-tephra mixture density is given by:

$$\varepsilon_\rho = \sqrt{\left(\frac{\delta Q_{Mdif}}{Q_{Mdif}}\right)^2 + \left(\frac{\delta Q_{Madv}}{Q_{Madv}}\right)^2 + \frac{1}{2} \left(\frac{\delta r_v}{r_v}\right)^2 + \left(\frac{\delta v_{ex}}{v_{ex}}\right)^2} \quad (6)$$

where we assume the same values for each independent parameter and $\delta v_{ex} = 0.20v_{ex}$, the relative percentage error ε_ρ is equal to 24%.

E. Time-Integrated Eruption Mass and Volume

We can introduce a quantity complementary to Q_M , named volume eruption rate and indicated by Q_V , due to pyroclastic material moving through surface per unit time, that can be retrieved if H_{TP} derived by XWR is known, applying the Mastin *et al.* relation [26] $Q_V = aH_{TP}^b$ with the coefficients a and b equal to 0.4786 and 3.512, respectively. It is possible to convert the estimates of Q_M into Q_V through the relation $Q_V = Q_M/\rho_m$, assuming a magma density ρ_m of 2700 kg/m³.

Integrating Q_M and Q_V in the whole eruption time range Δt , we obtain the time-integrated eruption mass (TIEM) and the time-integrated eruption volume TIEV. The last value of TIEM and TIEV at the end of the eruption event represents the total erupted mass (TEM) and total erupted volume (TEV) of the eruptive event.

IV. MASS ERUPTION RATE RETRIEVALS

In this section we present and analyze the Q_M estimates, derived by processing the XWR, VDR, and TIC measurements.

To compare retrieval methodologies and evaluate their differences for the eruptive events on 3–5 December 2015, we plot Q_M and Q_V in Fig. 7. In panels (a1)–(a4), we show the Q_M and Q_V estimates as a function of time t , derived from: (i) TPA methods, i.e., using the top-plume altitude H_{TP} , retrieved from the XWR within the DB12 model; ii) MCA method, and iii) NSA method, both derived from the XWR measurements. The retrievals, obtained using only the SFA method with $\rho_x = 7.5$ kg/m³, are shown in panels (b1)–(b4). They use the v_{ex} retrieved from the TIC and XWR (inverting the Torricelli relation) and v_{ex} directly derived from the VDR. Each value is sampled every 10 min, which is the minimum common sampling time imposed by the XWR operational schedule. The Q_M and Q_V retrievals are plotted with colored solid lines, whereas the uncertainties are expressed as colored areas around each method and limited by dashed lines in the same color, following the relation $Q_M \pm (\varepsilon_Q Q_M)$, where ε_Q is expressed as decimal value between 0 and 1.

For the event of 3 December 2015, the lower Q_M and Q_V climax values of about 2.010⁶ kg/s and 0.810³ m³/s, which are the values relating the transition to stable fountains [21], are estimated with the NSA. Because v_{ex} is similar among the three sensors, the temporal trends of the 3 SFA estimates are similar between 02:00 UTC and 03:30 UTC (2–1.810⁶ kg/s during climax). The Q_M (Q_V) retrievals derived from the TPA and MCA methods during the climax vary between 2.5 and 4.210⁶ kg/s (1.0 – 1.610³ m³/s), in agreement with the independent climax Q_M estimate of 2.710⁶ kg/s obtained by combining VDR echo power and velocities [21]. The uncertainties, plotted as colored areas in Fig. 7, are minimal among the SFA methods (about 0.510⁶ kg/s). Instead, the uncertainties of methods completely based on the XWR show some differences, about $\pm 1.010^6$ kg/s for the MCA and $\pm 0.510^6$ kg/s for the NSA; in particular, the NSA method tends to underestimate Q_M and associated uncertainty due to the uncertainty in the estimated area A_{NS} .

For the paroxysm of 4 December 2015, during the climax (09:10 – 10:00 UTC), the trends of Q_M and Q_V range between 0.5 and 1.910⁶ kg/s (0.3–0.710³ m³/s) for the MCA and TPA methods and come closer near the peak in Q_M at 09:20 (1.510⁶ kg/s versus 1.910⁶ kg/s, respectively). The NSA shows a time shift with a higher peak at 09:30 UTC of 2.310⁶ kg/s [see Fig. 7(a2)]. The SFA approaches vary from 0.7 to 1.210⁶ kg/s (0.2 – 0.510³ m³/s). In this case, the estimate using the velocity derived from VDR seems lower than others, probably due to a reduced v_{ex} retrieval for a pointing that does not perfectly intercept the region above the eruptive crater.

The eruptive event of the evening of 4 December 2015 starts from 20:10 to 21:40 UTC. For this event, the Q_M and Q_V peak retrievals range between 1.210⁶ kg/s and 2.210⁶ kg/s (0.410³ and 0.810³ m³/s) for the MCA, TPA, and NSA methods. Once again, the NSA estimate is delayed with a peak value at 21:00 UTC, 20 min after the MCA and TPA. Regarding the SFA methods, the Q_M and Q_V values range between 0.610⁶ and 1.810⁶ kg/s (0.210³ m³/s – 0.610³ m³/s). Regarding TIC, the presence of meteorological clouds at the summit between 20:20 and 20:50 UTC prevented the continuous determination of Q_M and Q_V with only one peak value at 20:40 (1.210⁶ kg/s and 0.510³

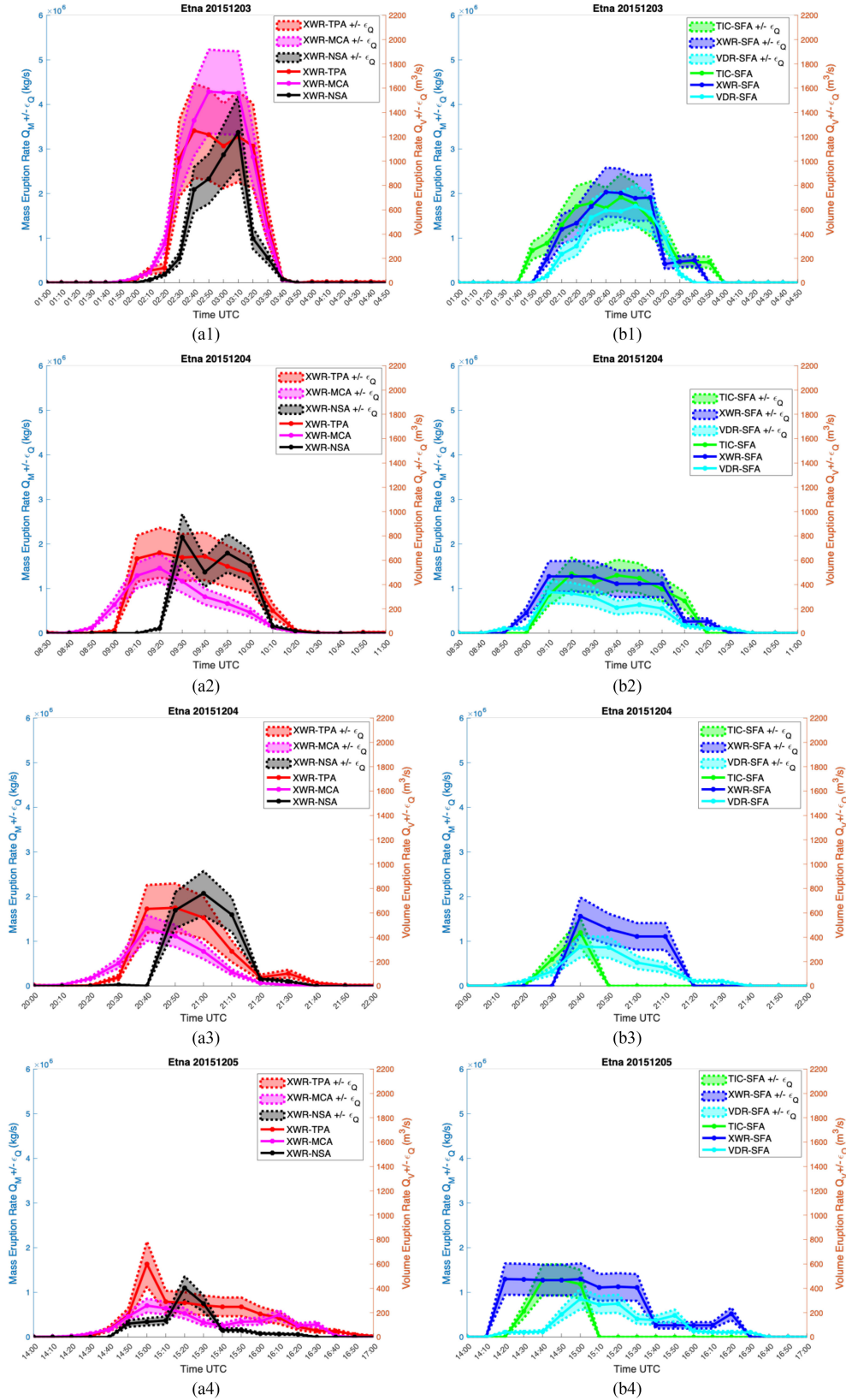


Fig. 7. Evolution of Q_M (kg/s) and Q_V (m³/s), axis on the right and on the left of each panel, respectively, and the relative uncertainties identified by the colored area bounded by dashed lines around each estimate (solid line) on (a1, b1) 3 December 2015, (a2, b2) 4 December 2015, (a3, b3) 4 December 2015, and (a4, b4) 5 December 2015. The left panels indicate the Q_M and Q_V retrievals, sampled every 10 min (and then linearly interpolated), as a function of time t , derived from: TPA methods, i.e., using the top-plume altitude H_{TP} retrieved from the XWR within the parametric relationships DB12 (setting a wind velocity of 7 m/s); MCA and NSA methods, both derived from the XWR elaboration. On the right panels, the retrievals are deduced from SFA methods using the exit velocity obtained from TIC, XWR, and VDR, respectively.

m^3/s , respectively). The SFA-VDR highlights a trend with lower values than TIC and XWR between 20:10 and 21:40 UTC.

Finally, for the event of 5 December 2015, the paroxysm lasts from 14:20 to 17:00 UTC. In this case, the TIC estimates are restricted to 14:20–15:10 UTC. During the climax, the Q_M and Q_V range between 0.7 and 1.310^6 kg/s (0.210^3 – 0.510^3 m^3/s) for the SFA approaches. For the SFA-XWR and SFA-VDR, the time range of Q_M and Q_V begins around 14:10 UTC and ends at 16:40 UTC. For the MCA we observe a lower Q_M (Q_V) estimation with a maximum of 0.710^6 kg/s (about 0.210^3 m^3/s) at 15:00 UTC. The TPA method shows greater Q_M and Q_V values with respect to the MCA and NSA, with a peak at 15:00 UTC. The NSA peak (1.210^6 kg/s, i.e., 0.410^3 m^3/s) is again delayed by about 20 min. In comparison with previous cases, we observe a lower agreement among the different trends. In particular, the SFA-TIC shows a trend that differs more from the others due to the limited ability of the sensor to observe the same eruptive event under cloud cover conditions. The SFA-XWR shows a greater trend in terms both of estimated values and of time interval compared to the other methods. This is related to the specific sensitivity of the sensor in observing the eruptive event in its temporal evolution.

In all cases previously described, the maximum Q_M and Q_V estimates are derived from the TPA (DB12) for 3 and 5 December, whereas for both events on 4 December the maximum is obtained with the NSA. The TPA method depends on both meteorological data (pressure, wind velocity, etc.) and mainly H_{TP} estimates derived from the XWR. Generally, when the visibility of each sensor is not degraded, a good agreement of the respective MER is noted. The Q_M peak values are generally in the same time instants for three employed sensors, except for the NSA, which shows a time delay in estimating the peak of the event related to the variation in time of the surface area crossed by the mass flow near the crater. The different trend of Q_M and Q_V retrievals, observed on 5 December 2015, is confirmed by the analysis of the thermodynamic variables derived from the radio sounding in Trapani, where a decrease of both temperature and atmospheric pressure is observed at an altitude of about 4 km asl event, again due to the flow area.

To analyze the correlation among Q_M estimates, we show in Fig. 8 the dispersion of the Q_M retrievals for the four eruptive events of Etna: Q_M from the NSA, TPA, and SFA (TIC, VDR, and XWR) methods are reported as a function of the Q_M from the MCA method. The NSA method shows a smaller dynamic, whereas the TPA method covers a larger set of Q_M values, although with wider scattering for low Q_M . Although equally distributed around the 1:1 line, the SFA methods display a more asymmetrical distribution with respect to the MCA. This is since v_{ex} does not vary much among paroxysms; in fact, we have a larger dynamic in the parameters that are related to the quantity of detected tephra (echo power, radar reflectivity factor, etc.) hence, unlike the MCA, SFA values are less varying among all paroxysms [42].

Note the particularly good agreement of the SFA-VDR with the MCA-XWR for Q_M above 610^4 kg/s.

As mentioned in Section III-C, the knowledge of MCA Q_M allows us to compute the eruptive crater radius r_v , through a

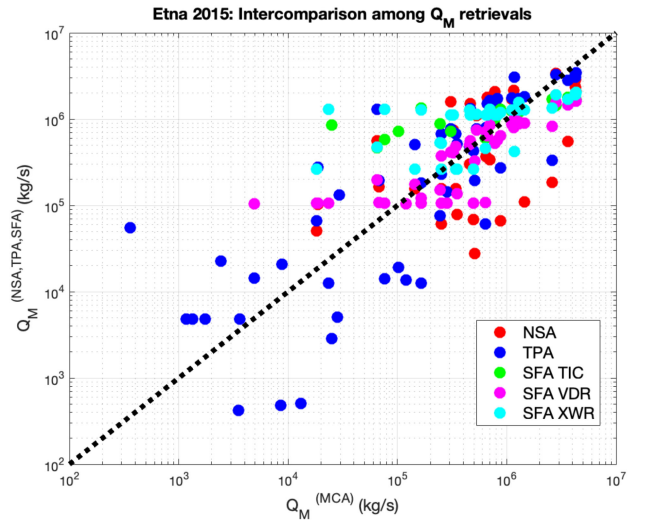


Fig. 8. Plot showing on the x -axis Q_M derived from the MCA method and on the y -axis Q_M retrieved from the NSA, TPA, and the three SFA methods, identified by different colored dots for the four Etna lava fountain events.

power regressive law, and the gas-tephra mixture density ρ_x . Fig. 9 shows the time trend of ρ_x as a function of time.

The red area bounded by the red dashed line identifies the value computed combining (5) and (6), that is $\rho_x \pm (\varepsilon_\rho \rho_x)$, where ε_ρ is expressed as decimal value between 0 and 1. The dashed red lines define the variability of ρ_x derived from the MCA density (green dashed line). Important variations, up to 25 kg/m^3 during purely volcanic signals, occur as a function of eruption time both for the TPA-derived and MCA-derived ρ_x , with larger averaged values for the former. The constant mixture density value, computed as the average of the mixture density derived by the MCA and TPA, is used in the SFA methods in Figs. 7 and 8. Across all four paroxysms, this averaged value ranges between 4 and 12 kg/m^3 , as a function of particle fraction f_N previously fixed [18], [39], [40]. We observe higher values of ρ_x during the last event when meteorological clouds covered Etna's summit area (especially after 15:30 UTC), as confirmed by the radio sounding and TIC images. In this case ρ_x represents the combined contributions of volcanic particles and hydrometeors.

V. SUMMARY AND COMPARISON OF Q_M AND Q_V RESULTS

We summarize the results derived from each retrieval approach, comparing them with data available in literature, to highlight congruencies and identify the potential of the various approaches.

Tables II and III show the time-averaged value of $\overline{Q_M}$ (kg/s) and $\overline{Q_V}$ (m^3/s) and the TEM (kg) and TEV (m^3), respectively, for Etna's paroxysms on 3–5 December 2015.

In the table, row *a* shows the values derived from the TPA model (DB12), whereas rows *b*–*d* refer to SFA using the video TIC, XWR, and VDR, respectively. Rows *e* and *f* show the results

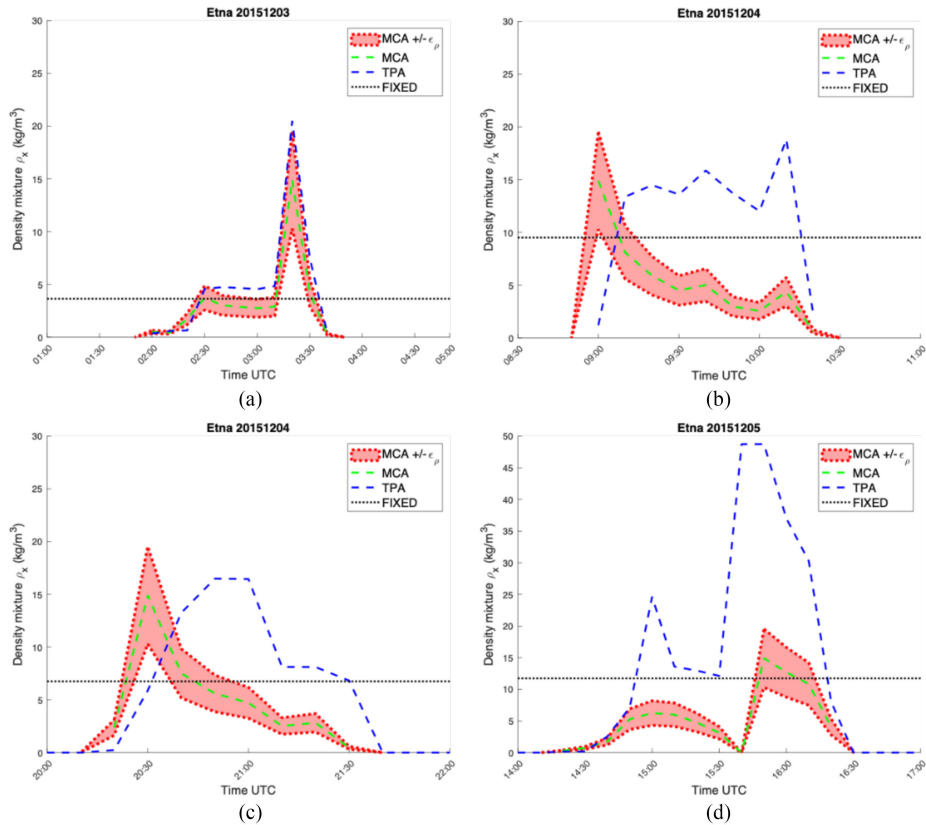


Fig. 9. Time trend of gas and tephra mixture density: the red area identifies the mixture density uncertainty computed according to the relation $\rho_x \pm \epsilon_\rho$, whereas the dashed green and blue lines are related to ρ_x using Q_M derived from MCA and TPA methods, respectively. The fixed value, plotted with a dashed dark line is obtained by averaging both estimates. Each picture is related to (a) 3 December 2015, (b) 4 December 2015 (06:30–11:00 UTC), (c) 4 December 2015 (20:00–22:00 UTC), and (d) 5 December 2015.

for the MCA and NSA retrievals, whereas the rows g , h , and i show the values derived from literature [20], [21].

For 3 December 2015, $\overline{Q_M}$ and $\overline{Q_V}$ time-averaged values in [20] and [21] and MCA-XWR values are larger than other estimates in this study, up to a factor 2 to 3 with respect to SFA methods (extrema: 4.510^6 kg/s for SFA-VDR, 14.510^6 kg/s in [21]). For both eruptions of the 4 December, the highest estimates are obtained with the TPA. For the 5 December, the approach that shows the largest time-averaged Q_M value is the SFA-XWR. Generally, the TPA model, when it has both reliable environmental data and measurements of the wind speed in function of the altitudes, shows time-averaged $\overline{Q_M}$ values that concur with the other estimates. In between, the SFA-XWR estimates retrieved from real-time XWR data show generally medium–high values between 3.910^5 and 610^5 kg/s . The MCA method, if the advection term is neglected, tends to show lower time-averaged $\overline{Q_M}$ and $\overline{Q_V}$. The NSA method provides estimates of time-averaged $\overline{Q_M}$ between MCA and TPA ones.

It is noteworthy that the differences with the time-averaged estimates in [20] remain unchanged in each case study analyzed independently from the considered approach. This is also the case for the TEM and TEV shown in Table III. On 3 December the largest values are noted with the TPA, SFA-TIC, and SFA-XWR techniques; on 4 December morning and evening with the TPA and SFA-XWR. Again, the TPA model displays the largest values with respect to other approaches, whereas on 5 December the larger value is with SFA-XWR.

In Table IV we listed the four Q_M approaches with their respective equations and extrapolated uncertainties. The MCA method is the one with the lowest overall uncertainty of about 22%, followed by the NSA method (26%), TPA (30%), and finally SFA (32%). The MCA method is more self-consistent from the radar point of view, as it is less dependent on parameters derived from other sensors and/or geophysical hypotheses formulated *a priori*. Mainly for this reason, the uncertainty associated with the MCA Q_M estimation is lower with respect to other Q_M estimates. The correlation matrix related to the Q_M retrievals is shown in Table V, where the coefficient values are always positive and the correlation between pairs of Q_M retrievals is highlighted by colored boxes. The highest correlation is observed between the SFA-VDR and both the TPA (0.94) and MCA (0.92), the lowest values are for the NSA and SFA-TIC (~ 0.4). Among the SFA approaches, the SFA-VDR shows the best correlation with the MCA and TPA methods, both trained by input parameters derived from the XWR, whereas the NSA has the lowest correlation. The TPA method is more correlated to the MCA and NSA methods, as well as the SFA-XWR and SFA-VDR.

VI. CONCLUSION

In this work, we analyzed the Etna paroxysms on 3–5 December 2015 to investigate and optimize the different strategies for Q_M and Q_V estimation and the related TEM and TEV as

well as their uncertainties. Starting from the three methodologies already known in the literature (MCA, TPA, and SFA), a new NSA approach was introduced and tested. For each method, advantages and limits were also discussed. A comparison between the various retrieval approaches, in terms of Q_M , Q_V , TEM, and TEV, and corresponding data available in the literature was carried out to highlight similarities and differences.

Using ground *in situ* measurements, the analysis of this event showed that the MCA method has the lowest uncertainty of 22.3%, whereas other approaches exhibited a higher uncertainty (i.e., 26.4% for NSA, 30% for TPA, and 31.6% for SFA). If weather radar observations are not available, the other approaches are valuable to derive a first reliable MER. The TPA method generally showed the largest MER retrieved values because it is particularly sensitive to the H_{TP} estimates that are influenced by the cross wind variability and consequent plume bending. The SFA-based results were consistent with each other, but significantly dependent on the estimate of the tephra exit velocity. Regarding the NSA method, entirely based on XWR, a more accurate estimate of the tephra flow crossing area just above the crater should improve its overall accuracy in the MER retrieval.

The MER retrieval methods, described and applied in this work, showed promising results that can be exploited to improve the tephra dispersal and fallout forecast at Etna in near real time. The potential of the remote sensors in operating both individually and in synergy with the other instruments should be further investigated using other case studies, where all sensors are contemporarily available. The high correlation of MER retrievals between XWR and VDR is particularly promising since it confirms the potential of XWR as scanning operational systems for volcanic eruption monitoring and near-source parameter estimation. Further work might be devoted to explore new techniques, using low-cost sensors for MER estimation and employing microwave radars as validation tools.

ACKNOWLEDGMENT

The authors would like to thank for the operation of VOLDORAD-2B radar of OPGC on Etna in close collaboration with INGV-OE (M. Coltelli, M. Prestifilippo). VOLDORAD-2B processed data are made available by OPGC in the framework of EPOS with support of EUROVOLC. We also thank the Italian Department of Civil Protection (DPC, Italy) for the provision of the X-band radar data.

REFERENCES

- [1] R. S. J. Sparks *et al.*, *Volcanic Plumes*, 1st ed. Hoboken, NJ, USA: Wiley, 1997.
- [2] M. Poret *et al.*, "Reconstructing volcanic plume evolution integrating satellite and ground-based data: Application to the 23rd November 2013 Etna eruption," *Atmos. Chem. Phys. Discuss.*, vol. 18, 2018, Art. on 7.
- [3] C. Bonadonna *et al.*, "Tephra sedimentation during the 2010 Eyjafjallajökull eruption (Iceland) from deposit radar and satellite observations," *J. Geophys. Res.*, vol. 116, 2011, Art. no. B12202.
- [4] F. S. Marzano *et al.*, "Near-real-time detection of tephra eruption onset and mass flow rate using microwave weather radar and infrasonic arrays," *IEEE Trans. Geosci. Remote Sens.*, vol. 54, no. 11, pp. 6292–6306, Nov. 2016.
- [5] S. Corradini *et al.*, "A multi-sensor approach for volcanic ash cloud retrieval and eruption characterization: The 23 November 2013 Etna Lava fountain," *Remote Sens.*, vol. 8, 2016, Art. no. 58.
- [6] L. Mereu, F. S. Marzano, M. Montopoli, and C. Bonadonna, "Retrieval of tephra size spectra and mass flow rate from C-band radar during the 2010 Eyjafjallajökull eruption Iceland," *IEEE Trans. Geosci. Remote Sens.*, vol. 53, no. 10, pp. 5644–5660, Oct. 2015.
- [7] S. Scollo *et al.*, "Volcanic ash concentration during the 12 August 2011 Etna eruption," *Geophys. Res. Lett.*, vol. 42, pp. 2634–2641, 2015.
- [8] B. Behncke, S. Branca, R. A. Corsaro, E. De Beni, L. Miraglia, and C. Proietti, "The 2011–2012 summit activity of Mount Etna: Birth, growth and products of the new SE crater," *J. Volcanol. Geothermal Res.*, vol. 270, pp. 10–21, 2014.
- [9] D. Carbone, L. Zuccarello, A. Messina, S. Scollo, and H. Rymer, "Balancing bulk gas accumulation and gas output before and during lava fountaining episodes at Mt. Etna nature 2015," *Sci. Rep.*, vol. 5, 2015, Art. no. 18049.
- [10] G. Carazzo, E. Kaminski, and S. Tait, "On the rise of turbulent plumes: Quantitative effects of variable entrainment for submarine hydrothermal vents, terrestrial and extra-terrestrial explosive volcanism," *J. Geophys. Res.*, vol. 113, 2008, Art. no. B09201.
- [11] L. Scharff, M. Hort, and N. R. Varley, "Pulsed Vulcanian explosions: A characterization of eruption dynamics using Doppler radar," *Geology*, vol. 43, pp. 995–998, 2015.
- [12] A. Y. Borisova, J. P. Toutain, A. Stefansson, S. Gouy, and P. de Parseval, "Processes controlling the 2010 Eyjafjallajökull explosive eruption," *J. Geophys. Res.*, vol. 117, 2012, Art. no. B05202.
- [13] A. Bonaccorso, S. Calvari, A. Linde, and S. Sacks, "Eruptive processes leading to the most explosive lava fountain at Etna volcano: The 23 November 2013 episode," *Geophys. Res. Lett.*, vol. 41, pp. 4912–4919, 2014.
- [14] L. Mereu, S. Scollo, S. Mori, A. Boselli, G. Leto, and F. S. Marzano, "Maximum-likelihood retrieval of volcanic ash concentration and particle size from ground-based scanning lidar," *IEEE Trans. Geosci. Remote Sens.*, vol. 56, no. 10, pp. 5824–5842, Oct. 2018.
- [15] G. Dubosclard *et al.*, "Doppler radar sounding of volcanic eruption dynamics at Mount Etna," *Bull. Volcanol.*, vol. 66, pp. 443–456, 2004.
- [16] A. E. Parfitt, "A discussion of the mechanisms of explosive basaltic eruptions," *J. Volcanol. Geothermal Res.*, vol. 134, pp. 77–107, 2004.
- [17] A. Spanu, M. De' Michieli Vitturi, and S. Barsotti, "Reconstructing eruptive source parameters from tephra deposit: A numerical approach for medium-sized explosive eruptions," *Bull. Volcanol.*, vol. 78, Sep. 2015, Art. no. 59.
- [18] F. S. Marzano, L. Mereu, S. Scollo, F. Donnadieu, and C. Bonadonna, "Tephra mass eruption rate from ground-based X-band and L-band microwave radars during the November 23, 2013 Etna paroxysm," *IEEE Trans. Geosci. Remote Sens.*, vol. 58, no. 5, pp. 3314–3327, May 2020.
- [19] T. Dürig *et al.*, "Earth, mass eruption rates in pulsating eruptions estimated from video analysis of the gas thrust-buoyancy transition—A case study of the 2010 eruption of Eyjafjallajökull, Iceland," *Planets Space*, vol. 67, 2015, Art. no. 180.
- [20] G. Vulpiani, M. Ripepe, and S. Valade, "Mass discharge rate retrieval combining weather radar and thermal camera observations," *J. Geophys. Res. Solid Earth*, vol. 121, pp. 5679–5695, 2016.
- [21] V. Freret-Logeril *et al.*, "Mass eruption rates of tephra plumes during the 2011–2015 lava fountain paroxysms at Mt. Etna from Doppler radar retrievals," *Front. Earth Sci.*, vol. 6, 2018, Art. no. 73.
- [22] V. N. Bringi and V. Chandrasekar, *Polarimetric Doppler Weather Radar*. Cambridge, U.K.: Cambridge Univ. Press, 2004.
- [23] L. Wilson and G. P. L. Walker, "Explosive volcanic eruptions ejecta dispersal in plinian eruptions: The control of eruption conditions and atmospheric properties," *Geophys. J. Int.*, vol. 89, no. 2, pp. 657–679, May 1987.
- [24] F. S. Marzano, S. Barbieri, E. Picciotti, and S. Karlsdóttir, "Monitoring sub-glacial volcanic eruption using C-band radar imagery," *IEEE Trans. Geosci. Remote Sens.*, vol. 48, no. 1, pp. 403–414, Jan. 2010.
- [25] F. S. Marzano, E. Picciotti, G. Vulpiani, and M. Montopoli, "Synthetic signatures of volcanic ash cloud particles from X-band dual-polarization radar," *IEEE Trans. Geosci. Remote Sens.*, vol. 50, no. 1, pp. 193–211, Jan. 2012.
- [26] L. G. Mastin *et al.*, "A multidisciplinary effort to assign realistic source parameters to models of volcanic ash-cloud transport and dispersion during eruptions," *J. Volcanol. Geothermal Res.*, vol. 186, pp. 10–21, 2009.
- [27] M. I. Mishchenko, "Calculation of the amplitude matrix for a nonspherical particle in a fixed orientation," *Appl. Opt.*, vol. 39, pp. 1026–1031, 2000.

- [28] B. R. Morton, G. Taylor, and J. S. Turner, "Turbulent gravitational convection from maintained and instantaneous sources," *Proc. Roy. Soc. London. Ser. A, Math. Phys. Sci.*, vol. 234, no. 1196, pp. 1–23, Jan. 1956.
- [29] L. Wilson and J. Head, "Ascent and eruption of basaltic magma on the Earth and Moon," *J. Geophys. Res.*, vol. 86, no. B4, pp. 2971–3001, Apr. 1981.
- [30] G. Dubosclard, R. Cordesses, P. Allard, C. Hervier, M. Coltelli, and J. Kornprobst, "First testing of a volcano Doppler radar (Voldorad) at Mount Etna, Italy," *Geophys. Res. Lett.*, vol. 26, pp. 3389–3392, 1999.
- [31] F. Donnadieu, "Volcanological applications of doppler radars: A review and examples from a transportable pulse radar in L-band," in *Doppler Radar Observations - Weather Radar, Wind Profiler, Ionospheric Radar, and Other Advanced Applications*. J. Bech and J. L. Chau, Eds., Rijeka, Croatia: InTech, 2012, pp. 409–446.
- [32] M. Rippepe, C. Bonadonna, A. Folch, D. Delle Donne, G. Lacanna, and B. Voight, "Ash-plume dynamics and eruption source parameters by infrared and thermal imagery: The 2010 eyjafjallajökull eruption," *Earth Planet. Sci. Lett.*, vol. 366, pp. 112–121, 2013.
- [33] W. Degruyter and C. Bonadonna, "Improving on mass flow rate estimates of volcanic eruptions," *Geophys. Res. Lett.*, vol. 39, 2012, Art. no. L16308.
- [34] E. Kaminski, S. Tait, F. Ferrucci, M. Martet, B. Hirn, and P. Husson, "Estimation of ash injection in the atmosphere by basaltic volcanic plumes: The case of the Eyjafjallajökull 2010 eruption," *J. Geophys. Res.*, vol. 116, 2011, Art. no. B00C02.
- [35] L. Wilson, R. S. J. Sparks, and G. P. L. Walker, "Explosive volcanic eruptions—IV. The control of magma properties and conduit geometry on eruption column behaviour," *Geophys. J. R. Astron. Soc.*, vol. 63, pp. 117–148, 1980.
- [36] S. Corradini *et al.*, "Proximal monitoring of the 2011–2015 Etna lava fountains using MSG-SEVIRI data," *Geosciences*, vol. 8, 2018, Art. no. 140.
- [37] L. Mereu, S. Scollo, C. Bonadonna, V. Freret-Lorgeril, and F. S. Marzano, "Multisensor characterization of the incandescent jet region of lava fountain-fed tephra plumes," *Remote Sens.*, vol. 12, 2020, Art. no. 3629.
- [38] R. A. Corsaro *et al.*, "Monitoring the December 2015 summit eruptions of Mt. Etna (Italy): Implications on eruptive dynamics," *J. Volcanol. Geothermal Res.*, vol. 341, pp. 54–69, 2017.
- [39] M. Trolese, M. Cerminara, T. E. Ongaro, and G. Giordano, "The footprint of column collapse regimes on pyroclastic flow temperatures and plume heights," *Nature Commun.*, vol. 10, 2019, Art. no. 2476.
- [40] T. Esposti Ongaro, J.-C. Komorowski, Y. Legendre, and A. Neri, "Modelling pyroclastic density currents from a subplinian eruption at la soufrière de Guadeloupe (West Indies, France)," *Bull. Volcanol.*, vol. 82, 2020, Art. no. 76.
- [41] C. Bonadonna, A. Costa, A. Folch, and T. Koyaguchi, *Tephra Dispersal and Sedimentation*. H. Sigurdsson, B. Houghton, H. Rymer, J. Stix, and, S. McNutt, Eds., Cambridge, MA, USA: Academic Press, 2015, p. 1456.
- [42] V. Freret-Lorgeril *et al.*, "Examples of multi-sensor determination of eruptive source parameters of explosive events at Mount Etna," *Remote Sens.*, vol. 13, 2021, Art. no. 2097.
- [43] S. Scollo *et al.*, "Near-real-time tephra fallout assessment at Mt. Etna, Italy," *Remote Sens.*, vol. 11, no. 2987, pp. 1–18, 2019.
- [44] F. Donnadieu, P. Freville, S. Rivet, C. Hervier, and P. Cacault, *The Volcano Doppler Radar Data Base of Etna (VOLDORAD 2B)*, Clermont-Ferrand, France: Université Clermont Auvergne-CNRS, 2015.
- [45] F. Donnadieu *et al.*, "Near-source Doppler radar monitoring of tephra plumes at Etna," *J. Volcanol. Geothermal Res.*, vol. 312, pp. 26–39, 2016.
- [46] M. Poret, A. Costa, D. Andronico, S. Scollo, M. Gouhier, and A. Cristaldi, "Modeling eruption source parameters by integrating field, ground-based, and satellite-based measurements: The case of the 23 February 2013 Etna paroxysm," *J. Geophys. Res., Solid Earth*, vol. 123, pp. 5427–5450, 2018.
- [47] M. Poret *et al.*, "Reconstructing volcanic plume evolution integrating satellite and ground-based data: Application to the 23 November 2013 Etna eruption," *Atmospheric Chem. Phys.*, vol. 18, no. 7, pp. 4695–4714, 2018.
- [48] R. S. J. Sparks, "The dimensions and dynamics of volcanic eruption columns," *Bull. Volcanol.*, vol. 48, pp. 3–15, 1986.
- [49] P.-Y. Tourmigan *et al.*, "The initial development of transient volcanic plumes as a function of source conditions," *J. Geophys. Res., Solid Earth*, vol. 122, pp. 9784–9803, 2017.
- [50] H. Sigurdsson, B. Houghton, H. Rymer, and J. S. S. McNutt, *Encyclopedia of Volcanoes*. New York, NY, USA: Academic, 1999.



Luigi Mereu received the M.Sc. degree in telecommunication engineering and the Ph.D. degree in remote sensing from the Sapienza University of Rome, Rome, Italy, in 2012 and 2016, respectively.

In 2012, he joined the Department of Information Engineering, Sapienza University of Rome, Roma, Italy, and the Centre of Excellence CETEMPS, L'Aquila to cooperate on radar remote sensing of volcanic ash clouds within the ICT Ph.D. program. He was involved in the FUTUREVOLC European project started in 2012 and the Aphorism European project started in 2014. He is involved in the EUROVOLC European project started in 2017. He was Visiting Student with the Icelandic Meteorological Office, Reykjavik, in 2014; and the Istituto Nazionale di Geofisica e Vulcanologia-Osservatorio Etno, Catania in 2015 and 2019. His research interests include analysis and modeling of eruptive plume using different remote sensing systems. Prof. Mereu was the recipient of the IEEE GRS South Italy Award for the Best Master Thesis in remote sensing in 2012.



Simona Scollo received the degree in physics (with hon.) from the University of Catania, Catania, Italy, in 2002, and the Ph.D. degree in physical modeling for environmental protection from the Università Alma Mater Studiorum of Bologna, Bologna, Italy, in 2006.

She is currently a Researcher with the Istituto Nazionale di Geofisica e Vulcanologia, Osservatorio Etno, Linguaglossa, Italy. She was a Visiting Scientist with the University of Geneva in 2015; with the Dipartimento di Fisica, Università di Federico II, Napoli, Italy, in 2011; with the Jet Propulsion Laboratory (NASA), Pasadena, USA, in 2010; with the Barcellona Supercomputer Center in 2008; with the Joint Research Centre, Ispra, in 2005; with the Department of Geology and Geophysics School of Ocean and Earth Science and Technology at Manoa, Hawaii, in 2003 and 2005. She has authored or coauthored 35 papers in refereed international journals, and more than 80 presentations at international conferences and workshops. Her research interests include analysis of the dispersal and fallout processes of eruptive plumes during explosive eruptions; calibration, sensitivity analysis, and uncertainty estimation of ash dispersal models; laboratory and field experiments; development of a multidisciplinary system for the detection and monitoring of volcanic plumes, and analysis of explosive activity using different remote sensing techniques (e.g., radar, lidar, satellites, etc.).

Prof. Scollo was the Editor of a Special Issue in Atmospheric Emissions from Volcanoes, Scientific Committee for FisMat 2015, and a Co-Convenor and the Chairman in different sessions of the European Geosciences Union and International Union of Geodesy and Geophysics. She is a Referee for several international journals. She coordinated several projects and one of them, the VAMOS SEGURO project, was selected in 2012 as a "best practice" among several European Cooperation Projects. In 2011, she was the recipient of the Rittmann medal for young researchers in volcanology and in 2010 the paper Scollo *et al.* was selected for the "AGU Research Spotlight".

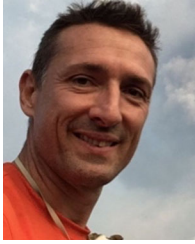


Costanza Bonadonna received the B.S. degree in geology from the University of Pisa, Pisa, Italy, in 1997, and the Ph.D. degree from the University of Bristol, Bristol, U.K, in 2001.

She was then awarded the position of Young Investigator at the University of Hawaii, and later appointed an Assistant Professor with the University of South Florida, Tampa, FL, USA. She is currently a Full Professor with the Department of Earth Sciences, University of Geneva, Geneva, Switzerland, where she is also the Vice-Dean of the Faculty of Sciences.

Her research interests include modeling sedimentation from volcanic plumes, exploring new methodologies for the characterization of tephra-fallout deposits, and developing probabilistic analysis for the assessment of volcanic hazards and risks.

Prof. Bonadonna was a recipient of the President's Award of the Geological Society of London (2001), the IAVCEI Outstanding Recent Graduate (2004), the Outstanding Woman in Science Award of the Geological Society of America (2004), the USF Outstanding Faculty Research Achievement Award (2005), and the International Galileo Galilei Award of the Italian Rotary Clubs for Sciences (2020). In addition, she is currently the president-elect of the Volcanology, Geochemistry, and Petrology section of the American Geophysical Union and a member of the Academia Europaea.



Franck Donnadieu received the Ph.D. degree in volcanology from the Université Clermont II, Clermont-Ferrand, France, in 2000.

Since 2002, he has been a Physician Adjoint with OPGC (Lab. Magmas et Volcans), Université Clermont Auvergne, Aubière, France, and was awarded the HDR diploma in 2017. After the Ph.D. he received the NSF Postdoctoral Fellowship with Penn State University (USA). He, then, spent one year with the Observatoire de Physique du Globe de Clermont-Ferrand to specialize in sounding of volcanic explosive eruptions using dedicated transportable radars. As part of the french SNOV (CNRS-INSU), he oversees a unique service (VOLDORAD) dedicated to volcanological Doppler radars comprising four instruments (3 UHF, 1 mm-wave) involved in ten campaigns, one radar being permanently monitoring Etna in collaboration with INGV-OE. He is also teaching courses in geophysics. His research interests include quantifying volcanic jets, plumes dynamics, and source parameters from radar remote sensing.

Prof. Donnadieu was the Coordinator of the UCA of the European MED-SUV program (2013–2016) and led the ash plume radar project of the ClerVolc Laboratory of excellence (2015–2018). He was the recipient of the three PEDR and one UCA awards for scientific excellence. Formerly a Member of the French CNAP and SNOV national committees, he is also a Member of IAVCEI, of the Scientific Board on Soufrière de Guadeloupe, of the UCA HDR diploma committee, and of the OPGC administration board.



Valentin Freret-Lorgeril received the Ph.D. degree in volcanology from the University Clermont-Auvergne (UCA), Clermont-Ferrand, France, in 2018.

Since 2019, he has been a Postdoc Researcher with the Department of Earth Sciences, University of Geneva, Geneva, Switzerland. He has been involved in the EUROVOLC European project started in 2017. His research interests include the determination of the eruptive source parameters of explosive eruptions using multisensor strategies, such as Doppler radars,

ground- and satellite-based infrared, or visible imagery; and the characterization of near real-time tephra sedimentation by optical disdrometers and ground-sampling.



Frank S. Marzano (Fellow, IEEE) received the master's degree in electronic engineering (with honors) and the Ph.D. degree in applied electromagnetics from the Sapienza University of Rome, Rome, Italy, in 1988 and 1993, respectively.

In 1992, he was a Visiting Scientist with Florida State University, Tallahassee, FL. During 1993, he collaborated with the Institute of Atmospheric Physics, National Council of Research (CNR), Rome, Italy. From 1994 to 1996, he was with the Italian Space Agency, Rome, Italy, as a Postdoctorate Researcher. After being a Lecturer with the University of Perugia, Italy, in 1997, he joined the Department of Electrical Engineering, University of L'Aquila, Italy, teaching courses on electromagnetic fields as an Assistant Professor. In 1999, he was with the Naval Research Laboratory, Monterey, CA, as a Visiting Scientist. In 2002, he qualified as an Associate Professor and has co-founded the Center of Excellence on Remote Sensing and Hydro-Meteorological Modeling (CETEMPS), L'Aquila. In 2005, he joined the Department of Information Engineering, Electronics and Telecommunications, Sapienza University of Rome, Rome, Italy, where he currently teaches courses on antennas, propagation, and remote sensing. He has authored or coauthored more than 130 papers in refereed international journals, more than 30 contributions to international book chapters, and more than 300 extended abstracts on international and national congress proceedings. His research interests include passive and active remote sensing of the atmosphere from ground-based, airborne, and space-borne platforms, and electromagnetic propagation studies.

Dr. Marzano, since 2007, has been a Vice-Director of CETEMPS with the University of L'Aquila, L'Aquila, Italy, where he was nominated as the Director in March 2013. He was the Editor of two books. From January 2004 until June 2014, he was an Associate Editor for the IEEE Geoscience Remote Sensing Letters (GRSL) and since mid-2014 he has been an Associate Editor for IEEE TRANSACTIONS ON GEOSCIENCE AND REMOTE SENSING (TGRS). In 2005 and 2007, he was a Guest Co-Editor of the *MicroRad04* and *MicroRad06* Special Issues for IEEE-TGRS. Since January 2011, he has been an Associate Editor for the journal *EGU Atmospheric Measurements Techniques*. He has been a Fellow of RMets (Royal Meteorological Society) since 2012 and a Fellow of IEEE since 2015.